Near-field terahertz imaging using sub-wavelength apertures without cutoff

Shuchang Liu,[1] Oleg Mitrofanov,[2] and Ajay Nahata[1]

[1]Department of Electrical and Computer Engineering, University of Utah, Salt Lake City, UT 84112, USA
[2]Department of Electronic and Electrical Engineering, University College London, London WC1E 7JE, UK,
[2]o.mitrofanov@ucl.ac.uk
[1]nahata@ece.utah.edu

Abstract: We demonstrate near-field imaging capabilities of a conical waveguide without cutoff using broadband terahertz (THz) radiation. In contrast to conventional conically tapered waveguides, which are characterized by strong suppression of transmission below the cutoff frequency, the proposed structure consists of two pieces, such that there is an adjustable gap along the length of the waveguide. We also ensure that the sidewalls are thin in the vicinity of the gap. The combination of these geometrical features allow for significantly enhanced transmission at frequencies below the cutoff frequency, without compromising the mode confinement and, consequently, the spatial resolution when used for imaging applications. We demonstrate near-field imaging with this probe simultaneously at several frequencies, corresponding to three regimes: above, near and below the cutoff frequency. We observe only mild degradation in the image quality as the frequency is reduced below the cutoff frequency. These results suggest that further refinements in the probe structure will allow for improved imaging capabilities at frequencies well below the cutoff frequency.

OCIS codes: (110.6795) Terahertz Imaging; (050.1220) Apertures; (260.3090) Infrared, far; (160.3900) Metals.

References and links

1. E. H. Synge, "A suggested method for extending microscopic resolution into the ultra-microscopic region," Philos. Mag. **6**, 356–362 (1928).
2. E. A. Ash and G. Nicholls, "Super-resolution aperture scanning microscope," Nature **237**, 510–512 (1972).
3. F. Zenhausern, M. P. O'Boyle, and H. K. Wickramasinghe, "Apertureless near- field optical microscope," Appl. Phys. Lett. **65**, 1623–1625 (1994).
4. Y. Inouye and S. Kawata, "Near-field scanning optical microscope with a metallic probe tip," Opt. Lett. **19**, 159-161 (1994).
5. A. Lewis, M. Isaacson, A. Harootunian, and A. Muray, "Development of a 500 Å spatial resolution light microscope: I. light is efficiently transmitted through λ/16 diameter apertures," Ultramicroscopy **13**, 227–231 (1984).
6. D. W. Pohl, W. Denk, and M. Lanz, "Optical stethoscopy: Image recording with resolution λ/20," Appl. Phys. Lett. **44**, 651-653 (1984).
7. H.-T. Chen, R. Kersting, and G. C. Cho, "Terahertz imaging with nanometer resolution," Appl. Phys. Lett. **83**, 3009–3011 (2003).
8. A. J. Huber, F. Keilmann, J. Wittborn, J. Aizpurua, and R. Hillenbrand, "Terahertz near-field nanoscopy of mobile carriers in single semiconductor nanodevices," Nano Lett. **8**, 3766–3770 (2008).
9. K. Moon, H. Park, J. Kim, Y. Do, S. Lee, G. Lee, H. Kang, and H. Han, "Subsurface nanoimaging by broadband terahertz pulse near-field microscopy," Nano Lett. **15**, 549–552 (2015).
10. T. L. Cocker, V. Jelic, M. Gupta, S. J. Molesky, J. A. J. Burgess, G. D. L. Reyes, L. V. Titova, Y. Y. Tsui, M. R. Freeman, and F. A. Hegmann, "An ultrafast terahertz scanning tunnelling microscope," Nat Photon **7**, 620–625 (2013).
11. S. Hunsche, M. Koch, I. Brener, and M. C. Nuss, "THz near-field imaging," Opt. Commun. **150**, 22–26 (1998).

12. O. Mitrofanov, M. Lee, J. W. P. Hsu, I. Brener, R. Harel, J. F. Federici, J. D. Wynn, L. N. Pfeiffer, and K. W. West, "Collection-mode near-field imaging with 0.5-THz pulses," IEEE Sel. Top. Quant. Electron. **7**, 600–607 (2001).
13. M. M. Awad and R. A. Cheville, "Transmission terahertz waveguide-based imaging below the diffraction limit," Appl. Phys. Lett. **86**, 221107 (2005).
14. H. Zhan, R. Mendis, and D. M. Mittleman, "Superfocusing terahertz waves below λ/250 using plasmonic parallel-plate waveguides," Opt. Express **18**, 9643–9650 (2010).
15. N. Klein, P. Lahl, U. Poppe, F. Kadlec, and P. Kužel, "A metal-dielectric antenna for terahertz near-field imaging," J. Appl. Phys. **98**, 014910 (2005).
16. K. Ishihara, K. Ohashi, T. Ikari, H. Minamide, H. Yokoyama, J. Shikata, and H. Ito, "Terahertz-wave near-field imaging with subwavelength resolution using surface-wave-assisted bow-tie aperture," Appl. Phys. Lett. **89**, 201120 (2006).
17. A. Bitzer and M. Walther, "Terahertz near-field imaging of metallic subwavelength holes and hole arrays," Appl. Phys. Lett. **92**, 231101 (2008).
18. O. Mitrofanov, C. C. Renaud, and A. J. Seeds, "Terahertz probe for spectroscopy of sub-wavelength objects," Opt. Express **20**, 6197 (2012).
19. Betzig, J. K. Trautman, T. D. Harris, J. S. Weiner, and R. L. Kostelak, "Breaking the diffraction barrier: optical microscopy on a nanometric scale," Science **251**, 1468–1470 (1991).
20. C. A. Balanis, *Advanced Engineering Electromagnetics* (John Wiley & Sons, 1989).
21. M. I. Stockman, "Nanofocusing of optical energy in tapered plasmonic waveguides," Phys. Rev. Lett. **106**, 019901 (2011).
22. T. D. Nguyen, Z. V. Vardeny, and A. Nahata, "Concentration of terahertz radiation through a conically tapered aperture," Opt. Express **18**, 25441–25448 (2010).
23. S. Liu, Z. V. Vardeny, and A. Nahata, "Concentration of broadband terahertz radiation using a periodic array of conically tapered apertures," Opt. Express **21**, 12363–12372 (2013).
24. S. Liu, O. Mitrofanov, and A. Nahata, "Transmission bleaching and coupling crossover in a split tapered aperture," Opt. Express **21**, 30895–30902 (2013).
25. A. J. Macfaden, J. L. Reno, I. Brener, and O. Mitrofanov, "3 micron aperture probes for near-field terahertz transmission microscopy," Appl. Phys. Lett. **104**, 011110 (2014).

.

1. Introduction

The ability to achieve spatial resolution beyond the diffraction limit [1,2] has proven to be an important tool for a variety of spectroscopic and imaging applications. This is generally accomplished using a variety of apertureless [3,4] and aperture-based [5,6] approaches. In the former category, high spatial resolution is achieved by bringing a sharply tapered wire in close proximity to the sample. Incident electromagnetic radiation is then concentrated on the sample surface by the wire tip and the scattered field is detected as the wire tip is scanned across the surface. Such techniques allow for very high spatial resolution, although the coupling (or scattering) efficiency tends to be low. In the terahertz (THz) spectral range, early work using this approach demonstrated spatial resolution on the order of λ/1000 [7-9]. More recent work has shown that significantly higher resolution is possible by detecting a THz field induced tunneling current between the tip and the sample [10]. Aperture-based techniques, on the other hand, do not typically allow for the same level of spatial resolution, but benefit from a relatively simple experimental configuration and the possibility of obtaining the THz field distribution near the sample surface without causing such strong field perturbation as occurs in the scattering tip method. In the simplest embodiment, the object is illuminated through a sub-wavelength aperture in a metallic screen. The aperture creates a sub-wavelength size light source, which is not limited by diffraction, but determined by the aperture size [1,2,3,11]. The sub-wavelength aperture can also be used for probing the optical field with sub-wavelength spatial resolution (~λ/100) [12]. It is worth noting that a variety of other structures have also been employed to perform near-field THz imaging [13-18]. For example, sub-wavelength size THz illumination sources were demonstrated using parallel plate waveguides. Small plate spacing allowed for sub-wavelength confinement along one axis [13], while tapered waveguide plates were shown to confine THz waves along both transverse axes to a level better than λ/145 [14]. Even stronger THz wave confinement was achieved using two sharp

needles [18]. These last two approaches overcome the main limitation of the aperture-type method: strong transmission suppression in the regime below the cutoff frequency.

In conventional optical near-field microscopy, high spatial resolution is commonly achieved by tapering an optical fiber and appropriately metallizing it such that there is a subwavelength aperture at the tip [19]. The aperture exhibits a cutoff frequency associated with its diameter [20]. At optical frequencies, where narrowband lasers are typically used, the aperture effect can be approximated by simple reduction of the overall transmissivity of the probe. On the other hand, for single-cycle pulses, which are often used for THz imaging, the aperture can cause strong pulse deformation [12]. Conically tapered structures should, in principle, also exhibit concentration of the incident radiation [21]. However, the observation of such effects is complicated by the lossy nature of metals at visible frequencies. Although tapered waveguides have previously been used for near-field THz imaging [11], detailed investigations of the concentrated field at the output of the structure is still missing in the literature. We have recently investigated the spectral and field concentration properties of conically tapered waveguides with sub-wavelength output apertures [22-24]. These structures, fabricated in a variety of different metals, all exhibit approximately similar behavior: (i) concentration of the incident THz electric field is maximized for a taper full angle of 30°, (ii) a reduction in group velocity occurs inside the conical waveguide [22], and (iii) THz transmission is suppressed below the cutoff frequency, f_c, associated with the output aperture diameter.

To mitigate this last effect, we fabricated a tapered waveguide with cylindrical apertures on the input and output faces in a metal block that was cut in half through the center of the structure [23]. The rationale for 'splitting' the waveguide and introducing a gap was that when the two halves were not electrically connected, they could support broadband transmission (TEM-like mode), as we confirmed experimentally. However, since this 'split' waveguide was effectively the superposition of a conical waveguide and a parallel plate waveguide, by virtue of being fabricated in a metal block, the introduction of even a very modest gap on the order of 10-20 μm allowed for a significant fraction of the field to leak into the gap and couple into the parallel plate waveguide mode, destroying the field confinement by the aperture. To maintain the confinement, we proposed and showed numerically that a split, tapered waveguide with thin (~60 μm) sidewalls, would minimize the field leakage [24].

In this work, we describe the fabrication and experimental transmission properties of such a structure, hereafter referred to as a conical waveguide with a sub-wavelength output aperture (CWSA). We also demonstrate its use for near-field imaging. The structure consists of two halves of a conically tapered waveguide with a variable gap. The tapered structure enables field concentration, broadband transmission and sub-wavelength spatial resolution set by the output aperture diameter, which we demonstrate using THz time-domain spectroscopy. Based on these results, we use the probe to image a U-shaped pattern fabricated into a thin metal foil at several different frequencies above and below the cutoff frequency of the CWSA. Further refinements in the structure should allow for high signal-to-noise near-field imaging well below the cutoff frequency.

2. Experimental details

We fabricated CWSAs using wire electrical discharge machining (wire EDM). Figure 1 shows schematic diagrams of the structure, along with the relevant geometrical parameters, and a photograph of the final probe. The CWSA was fabricated using a 3 mm thick stainless steel plate that was cut into two pieces and polished. Each half of the tapered aperture was then fabricated with a taper half-angle, relative to the propagation axis, of 15°. The bottom face of the probe was also tapered, with an angle of $\theta = 10°$, relative to the top plane, to minimize contact between the probe and the sample under test. The final device consisted of a conically tapered waveguide with a circular input aperture of a diameter $D_1 = 1.8$ mm, a length $d = 3.0$ mm and a taper full angle $\alpha = 30°$, which we have previously found to be the optimal taper angle [23]. The diameter of the circular output aperture was $D_2 = \sim 180$ μm, corresponding to a cutoff frequency $f_c = 1$ THz. Based on our findings from earlier simulation work [24], we

designed the thickness of the sidewalls near the gap to be 60 μm. The precision in the dimensions and surface roughness is shown in Fig. 1(d). The two halves of the device could be moved freely to allow for a variable gap g. In all of the following work, the incident and transmitted THz radiation was polarized perpendicular to the gap.

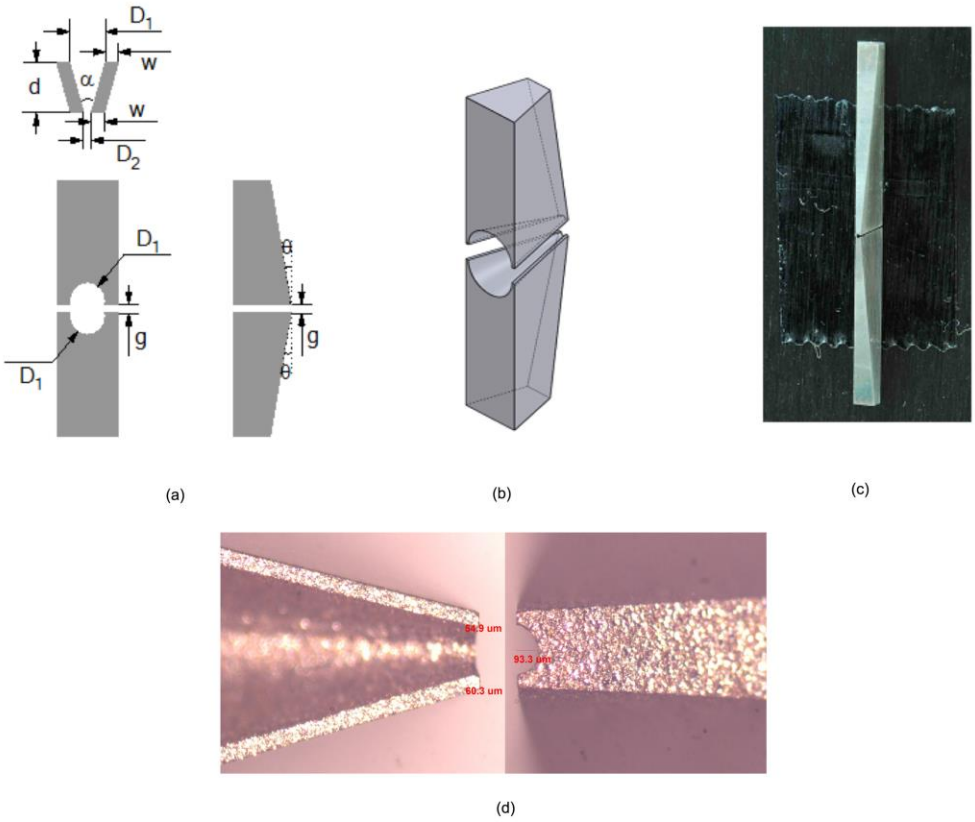

Fig. 1. Details of the CWSA. (a) Schematic cross-section (left top), top view (left bottom) and side view (right bottom) of the structure with an input aperture diameter, D_1 = 1.8 mm, an output aperture diameter, D_2 = 180 μm, probe length, d = 3.0 mm, and a taper full angle, α = 30°. The two halves of the aperture are separated by a variable gap spacing, g. The bottom plane of the device is also cut at an angle θ = 10° with respect to the top surface. The sidewall thickness at the gap on both sides is 60 μm. (b) Perspective view of the CWSA with a gap. (c) Photographs of the CWSA (with g ≈0). For the purposes of this image, the CWSA is attached to a planar surface using double-sided tape. (d) Images of half of the CWSA from the side (left) and bottom (right).

We characterized the probes experimentally using a THz time-domain spectroscopy and imaging setup shown in Fig. 2(a). The details of the system are described in [24] and discussed only briefly here. We used a ZnTe crystal to generate broadband THz radiation and a silicon lens to collect and focus the THz beam into the CWSA. This radiation was polarized perpendicular to the gap, analogous to what would be needed for broadband propagation in a parallel plate waveguide. The THz beam had a Gaussian spatial profile with a beam waist that occurred after the silicon lens at position *A*, as shown in Fig. 2(b). The input plane of the CWSA was placed at position B to ensure that the beam size was larger than the input aperture and, therefore, the incident field had a uniform distribution at the CWSA input. Two halves of the CWSA were aligned using an optical microscope and precision positioning stages resulting in the edge alignment accuracy better than 5 μm. The two halves were then brought to contact to close the gap between them. That position is identified throughout this

article as g = 0. We note however that the surface roughness prevents us from closing the gap along the entire edge of the structure. To increase the gap during the experiments, one of the CWSA halves was translated using the precision positioning stage. The transmitted THz radiation was detected at the output using a photoconductive dipole detector with a 10 μm aperture [25]. The CWSA was positioned in front of the photoconductive dipole detector using sub-micrometer precision translation stages. The CWSA was then moved away from the detector by 10 μm to avoid detection of field localization, which can occur due to surface roughness of the CWSA edges. In Fig. 2(c), we show the time-domain waveforms with and without the CWSA measured at point B, showing concentration by the CWSA.

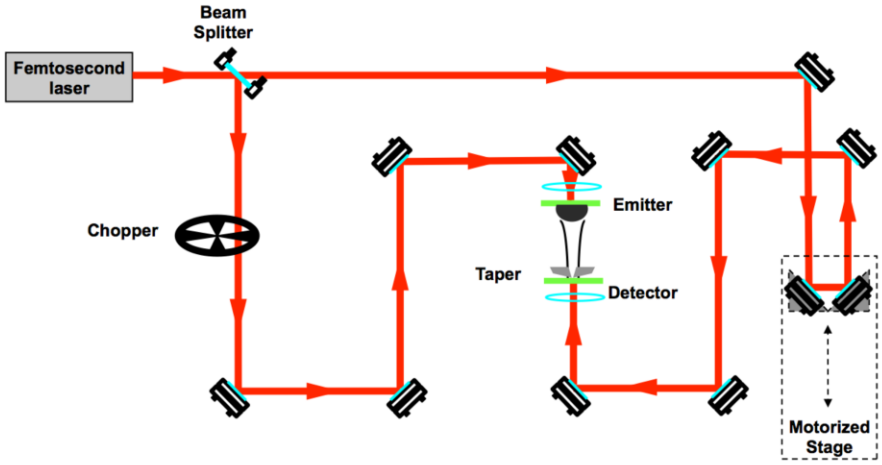

(a)

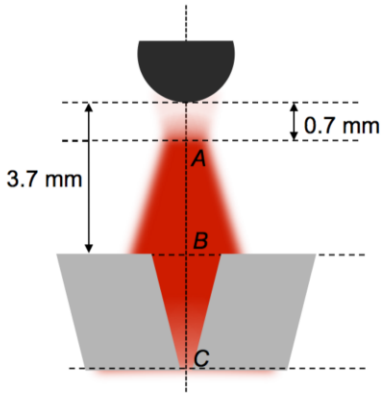

(b)

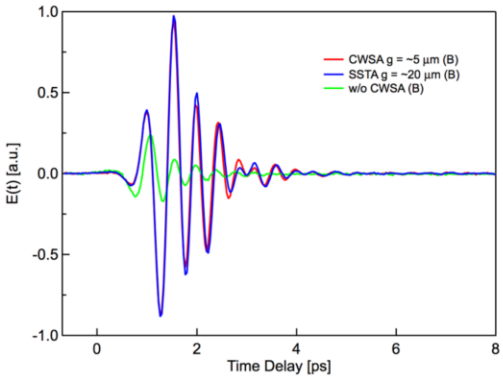

(c)

Fig. 2. Details of the experimental system. (a) Schematic diagram of the measurement system. Broadband THz radiation emitted from ZnTe was collected and focused, using a hyperhemispherical silicon lens, at normal incidence on the CWSA structure. The transmitted THz pulse was detected using the photoconductive probe with a 10 μm input aperture. (b) Enlarged diagram of the THz beam showing relevant positions of the components and the locations where measurements were taken. (c) Time domain waveforms measured at point B for three different circumstances.

3. Experimental results and discussion

We initially measured the spectral transmission properties of the CWSAs that had a 1.8 mm diameter input aperture and a 180 µm diameter output aperture for two different gap spacing values and compared these results to equivalent tapered apertures with no gap. These data are shown in Fig. 3, along with the measurements of the incident field. The corresponding positions of the probe are marked in Fig. 2 by letters *B* and *C*. Although the incident beam was divergent at the plane of the CWSA input, as shown in Fig. 2(b), all three tapered aperture configurations concentrate the field by a factor of ~3 compared to the field at the input of the aperture. For a CWSA with g = 0 µm, the spectrum is strongly suppressed at frequencies below the cutoff frequency of 1 THz, though the tapered nature of the structure ensures that there is not a sharp cutoff at that frequency [23]. For both CWSAs with non-zero gaps, lower frequencies are clearly enhanced relative to g = 0 µm. These CWSAs also exhibit a dip in the 1.5-1.75 THz region, which may be due to reflections within the complex structure. It is clear that even very small gaps allow for significant broadening of the transmitted THz spectrum. In fact, there appears to be relatively little difference between a CWSA with g = ~5 µm and g = ~20 µm. However, we found that for CWSAs with g values greater than ~20 µm, the transmission peak at ~2 THz becomes noticeably reduced. The transmission below 0.5 THz is relatively small in all three cases. In fact, the spectral amplitude in this low frequency regime is smaller than we expected based on numerical simulations (not shown). This may be the result of slight misalignment between the two pieces of the CWSA, as well as some surface roughness on the sidewalls that form the gap. Based on these findings, we use a gap of ~20 µm for all of the subsequent imaging work.

In Fig. 3(b), we show the relative phase difference for the two CWSAs relative to the incident radiation, which shows the dispersive effects of the tapered aperture. Only the data from 0.5 – 3.0 THz is shown here, because of the small spectral amplitude outside of this range. It is interesting to note that the two CWSAs have almost identical dispersion properties and that there is no strong modulation in the spectrum. Below the cutoff frequency, we would not expect any phase change through the CWSA, which would correspond to offset in the phase relative to the free space condition. However, because of the graded change in the aperture diameter through the taper, this offset is expected to be frequency dependent, which may account for the difference in slope up to ~1 THz. That analysis is beyond the scope of this manuscript.

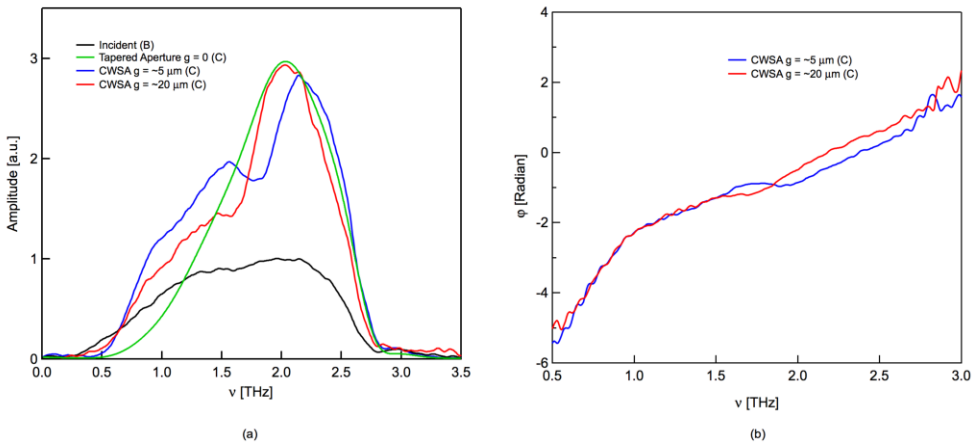

Fig. 3. Amplitude and spectra of the THz electric field incident and transmitted through the CWSAs for two different values of the gap spacing, g, and for a tapered aperture with g = 0. (a) Amplitude spectra for the three transmitted spectra are all scaled relative to the incident THz amplitude spectrum, which has a maximum value of 1. (b) Phase spectra showing the change in phase relative to the incident wave.

Figure 4 summarizes the basic spatial properties of the THz electric field measured approximately 10 μm from the output aperture of the CWSA. In order to properly assess these spatial properties, we initially measured the THz time-domain electric field properties across a 200 μm × 200 μm region centered about the CWSA. Figures 4(a) and 4(b) show space-time maps of the measured THz waveforms along the x- and y-axes, respectively. In both plots, the maximum of the THz pulse occurs at approximately t = 1.27 ps, regardless of the position within that region. Therefore, we can simply use the field magnitude at that temporal position to map out the THz electric field. In Figs. 4(c) and 4(d), we show the specific regions that were interrogated. Finally, in Figs. 4(e) and 4(f), we show the measured field distributions taken in 10 μm increments along both axes. It is clear that despite the 20 μm gap between the two portions of the CWSA, the THz electric field is strongly confined within the region of the output aperture. This is also consistent with earlier numerical simulations on similar structures [24]. To quantify this, we show the electric field profiles along the x- and y-axes measured through the center of the image in Fig. 4(e). The full-width at half-maximum (FWHM) of the THz intensity (proportional to the square of the THz electric field) is ~100 μm along both axes.

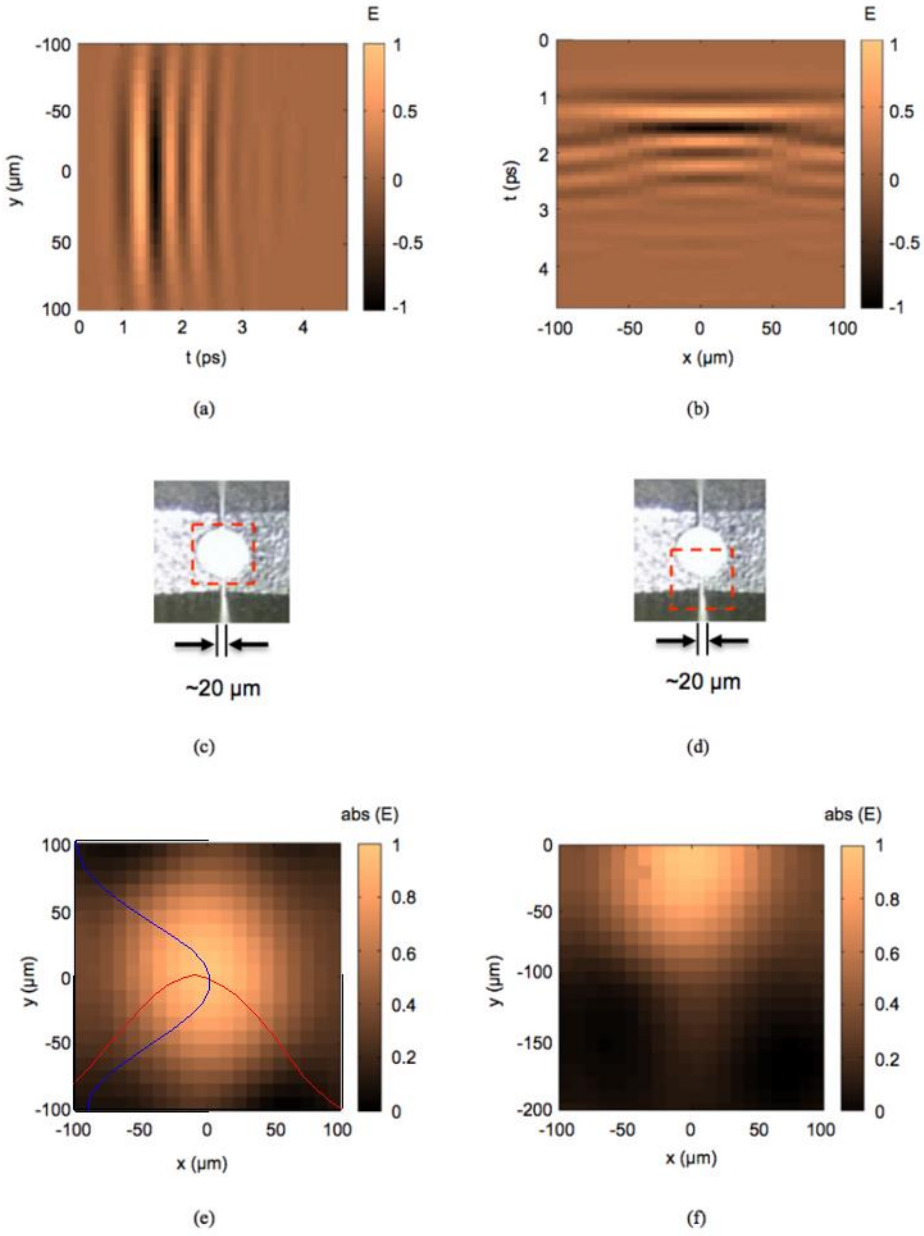

Fig. 4. THz electric field distribution at the CWSA output for g = 20 μm. (a, b) Space-time maps showing the transmitted THz pulse along the *x*-axis (*y* = 0) and along the *y*-axis (*x* = 0), respectively. (c, d) Photographs of the output aperture taken from the bottom of the CWSA with the region circled by the red square indicating the scanned regions in (e, f) respectively. Each pixel corresponds to the measured THz field at t = 1.27 ps. The overlaid red and blue curves in (e) show the electric field amplitudes along the *x*- and *y*- axes, respectively.

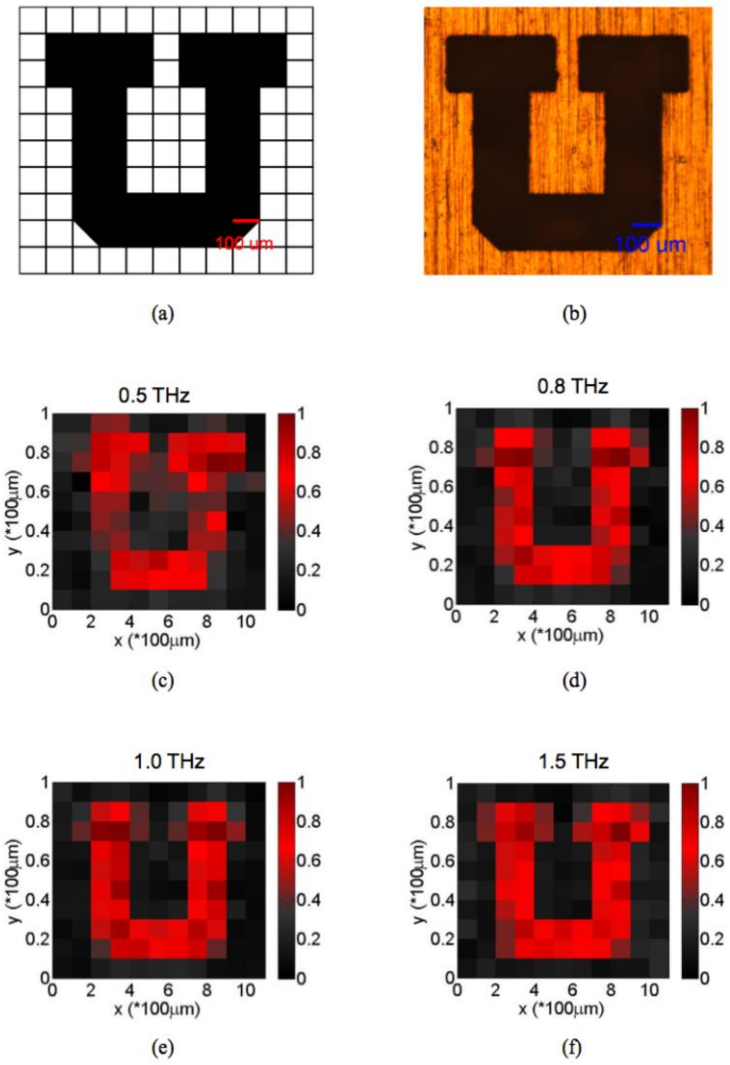

Fig. 5. Imaging using a CWSA with an output aperture diameter of 180 µm and a gap spacing of 20 µm. (a) Design of a U shaped test structure. (b) Photograph of the fabricated structure in a 75 µm thick free-standing stainless steel foil. Near field images of the structure at (c) 0.5 THz, (d) 0.8 THz, (e) 1.0 THz and (f) 1.5 THz.

Using the experimental system shown in Fig. 2(a), we now demonstrate the imaging capabilities of the CWSA. We fabricated a U-shaped test structure via laser ablation in a 75 µm thick free-standing stainless steel foil. A schematic diagram of the geometry is shown in Fig. 5(a) and a photograph of the sample is shown in Fig. 5(b). The sample was positioned <50 µm from the CWSA, and was scanned along both transverse axes in 100 µm increments, corresponding to the FWHM beam spot size for the THz intensity at the aperture output. For each pixel, we measured the THz time-domain waveform, Fourier transformed it, and used the resulting amplitude values at four separate frequencies (0.5 THz, 0.8 THz, 1.0 THz and 1.5 THz) to create false color images. These images are shown in Figs. 5(c)-5(f). While the image quality is reduced slightly with decreasing frequency, the image of the U is still clearly visible even for frequencies well below the cutoff frequency. It is worth noting that we were not able to obtain such images for frequencies below cutoff using a conventional tapered aperture (g = 0 µm).

4. Conclusion

In summary, we have demonstrated the utility of a split tapered waveguide with a sub-wavelength aperture for near-field THz imaging. The structure consists of two halves of a conventional conical waveguide, allowing for the introduction of a variable gap between the two pieces. By virtue of the narrow sidewalls in the vicinity of the gap, the structure allows for broadband THz propagation, maintains its ability to concentrate the incident THz radiation across that spectral range, and enables electric field confinement in a region determined by the output aperture. Based on these characteristics, we demonstrate near-field imaging of a U-shaped pattern fabricated in a metal foil at several different frequencies above and below the cutoff frequency. Further refinement in the fabrication of the probe should allow for improved imaging capabilities at even lower frequencies. The results suggest that this device may be useful for near-field imaging at frequencies well below the diffraction limit. Finally, we note that in contrast to photoconductive dipoles that have an integrated aperture [25], these tapered waveguides can be used with any type of incident THz radiation and, thus, are not limited to ultrafast optically generated THz radiation. While the dipoles with integrated apertures can provide higher spatial resolution, not every application allows such probes to be brought into sufficient proximity for high-resolution imaging.

Acknowledgments

This work was supported through the National Science Foundation MRSEC program under grant #DMR-1121252 and by the Royal Society under grant number UF130493.